Full Title:

Synthetic Heparan Sulfate Mimetic Pixatimod (PG545) Potently Inhibits SARS-CoV-2 By Disrupting The Spike-ACE2 interaction

Short title:

Heparan Sulfate Mimetic Pixatimod Potently Inhibits SARS-CoV-2

Authors

Scott E. Guimond[1,†], Courtney J. Mycroft-West[1,†], Neha S. Gandhi[2,†], Julia A. Tree[3,†], Karen R. Buttigieg[3], Naomi Coombes[3], Michael J. Elmore[3], Kristina Nyström[4], Joanna Said[4], Yin Xiang Setoh[5,6], Alberto A. Amarilla[5,6], Naphak Modhiran[5,6], Julian D.J. Sng[5,6], Mohit Chhabra[5,6], Daniel Watterson[5,6] , Paul R. Young[5,6], Alexander A. Khromykh[5,6], Marcelo A. Lima[1], Edwin A.Yates[7], Richard Karlsson[8], Yen-Hsi Chen[8], Yang Zhang[8], Edward Hammond[9], Keith Dredge[9], Miles W. Carroll[3,‡], Edward Trybala[4,‡], Tomas Bergström[4,‡], Vito Ferro[5,6,‡], Mark A. Skidmore[1,‡] and Jeremy E. Turnbull[7,8‡*]

[1]Molecular & Structural Biosciences, School of Life Sciences, Keele University, Newcastle-Under-Lyme, Staffordshire, ST5 5BG, UK.

[2]School of Chemistry and Physics, Centre for Genomics and Personalized Health, Queensland University of Technology, 2 George Street, Brisbane, QLD 4000, Australia.

[3]National Infection Service, Public Health England, Porton Down, Salisbury, Wiltshire, England, UK, SP5 3NU.

[4]Department of Infectious Diseases, Institute of Biomedicine, University of Gothenburg, Guldhedsgatan 10B, S-413 46 Goteborg, Sweden

[5]School of Chemistry and Molecular Biosciences, the University of Queensland, Brisbane, QLD 4072, Australia.

[6]Australian Infectious Diseases Research Centre, the University of Queensland, Brisbane, QLD 4072, Australia.

[7]Department of Biochemistry and Systems Biology, Institute of Systems, Molecular and Integrative Biology, University of Liverpool, Liverpool, L69 7ZB, UK.

[8]Copenhagen Center for Glycomics, Department of Cellular & Molecular Medicine, University of Copenhagen, Copenhagen N 2200, Denmark.

[9]Zucero Therapeutics Ltd, 1 Westlink Court, Brisbane, Queensland 4076, Australia.

[†]These authors contributed equally

[‡]Equal senior authors

[*]Corresponding author: j.turnbull@liverpool.ac.uk; +44 (0)151 795 4427

Summary

Heparan sulfate (HS) is a cell surface polysaccharide recently identified as a co-receptor with the ACE2 protein for recognition of the S1 spike protein on SARS-CoV2 virus, revealing an attractive new target for therapeutic intervention. Clinically-used heparins demonstrate relevant inhibitory activity, but world supplies are limited, necessitating a synthetic solution. The HS mimetic pixatimod is synthetic drug candidate for cancer with immunomodulatory and heparanase-inhibiting properties. Here we show that pixatimod binds directly to the SARS-CoV-2 spike protein receptor binding domain (S1-RBD), altering its conformation and destabilizing its structure. Molecular modelling identified a binding site overlapping with the ACE2 receptor site. Consistent with this, pixatimod inhibits binding of S1-RBD to ACE2-expressing cells and displays a direct mechanism of action by inhibiting binding of S1-RBD to human ACE2. Assays with four different clinical isolates of live SARS-CoV-2 virus show that pixatimod potently inhibits infection of Vero cells at doses well within its safe therapeutic dose range. This demonstration of potent anti-SARS-CoV-2 activity establishes that synthetic HS mimetics can target the HS-Spike protein-ACE2 axis. Together with other known activities of pixatimod our data provides a strong rationale for its further investigation as a potential multimodal therapeutic to address the COVID-19 pandemic.

198 words

Introduction

The coronavirus-19 disease (COVID-19) pandemic caused by the severe acute respiratory syndrome coronavirus 2 (SARS-CoV-2) has according to the World Health Organisation already surpassed 38 million cases and 1 million deaths world-wide. Given the severe pathophysiology induced by SARS-CoV-2 (*1*), the need for therapeutic alternatives to alleviate and stop the COVID-19 epidemic is clear. Heparan sulfate (HS) is a highly sulfated glycosaminoglycan found on the surface of most mammalian cells which is used by many viruses as an entry receptor or co-receptor (*2*), including coronaviruses (*3*). Various compounds that mimic cellular HS such as clinically-used heparins have been investigated and have been shown to block infectivity and cell-to-cell spread in a multitude of different viruses, including SARS-associated coronavirus strain HSR1 (*4*). The glycosylated spike (S) protein of SARS-CoV-2 mediates host cell invasion via binding to a receptor protein, angiotensin-converting enzyme 2 (ACE2) (*5*). Analysis of the sequence and experimentally determined structures of the S protein reveals that the receptor binding domain (RBD) of the S1 subunit contains a HS binding site. Recent studies have clearly demonstrated binding of heparin and HS to S1 RBD (*6-9*), including induction of significant conformational change in the S1 RBD structure (*6*), and also revealed that HS is a co-receptor with ACE2 for SARS-CoV2 (*10*). Collectively these data strongly suggest that blocking these interactions with heparins and HS mimetics has potential as an effective strategy for COVID-19 therapy. Although heparins have major potential for repurposing for such applications, limitations in the global supply of natural product heparins will greatly restrict its availability (*11*), highlighting an urgent need to find synthetic alternatives.

Pixatimod (PG545) is a clinical-stage HS mimetic with potent anti-cancer (*12,13*), and anti-inflammatory properties (*14*). However, significant antiviral and virucidal activity for pixatimod has also been reported against a number of viruses that use HS as an entry receptor with EC_{50}'s ranging from 0.06 to 14 µg/mL. This includes HSV-2 (*15*), HIV (*16*), RSV (*17*), Ross River, Barmah Forest, Asian CHIK and chikungunya viruses (*18*), and Dengue virus (*19*). *In vivo* efficacy has been confirmed in a prophylactic mouse HSV-2 genital infection model (*15*), a prophylactic Ross River virus mouse model (*18*) and a therapeutic Dengue virus mouse model (*19*). Pixatimod has been evaluated in a Phase Ia clinical trial in patients with advanced solid tumours where it demonstrated a tolerable safety profile and some evidence of disease control (*13*). It has been safely administered to over 80 patients pancreatic or bowel cancers in a Phase Ib study in combination with nivolumab (ACTRN12617001573347), prompting us to examine its anti-viral activity against SARS-CoV-2.

Here we provide evidence of a direct interaction of pixatimod with the S1 spike protein RBD, supported by molecular modelling data. Pixatimod was also able to inhibit the interaction of S1-RBD with ACE2 and also Vero cells (which are known to express the ACE2 receptor), indicating a direct mechanism of action. Finally we established that pixatimod is a potent inhibitor of attachment and invasion of Vero cells by multiple clinical isolates of live SARS-CoV-2 virus, and reduces its cytopathic effect, at concentrations within the known therapeutic range of this drug. Our data demonstrate that synthetic HS mimetics can target the HS-Spike protein-ACE2 axis, and provide strong support for clinical investigation of the potential of pixatimod as a novel therapeutic intervention for prophylaxis and treatment of COVID-19.

Results

Modelling of pixatimod-spike protein interactions

We initially used molecular dynamics (MD) simulations to map the potential binding sites of pixatimod (**Fig 1A**) on the S1 RBD surface (**Fig 1B**). A total of 24 unique residues of RBD were identified to be interacting with several residues of ACE2 based on the X-ray structures (**Fig 1B**). Amino acids making significant interactions with pixatimod were identified on the basis of their individual contributions to the total interaction energy, considering only the residues that contribute less than -1.0 kcal/mol. A number of these residues (Tyr489, Phe456, Leu455, Ala475) are also involved in binding to ACE2. The decomposition approach was helpful for locating residues of the RBD domain such as Lys458, Ser459, Lys462 and Asn481 that transiently interact to form hydrogen bonds or ionic interactions with the sulfated tetrasaccharide of pixatimod (**Fig 1D**). The free energy of binding is -10 kcal/mol, wherein van der Waals energies make the major favourable contribution to the total free energy. The cholestanol residue formed stabilizing interactions with Tyr489, Phe456, Tyr473, Ala475, Gln474 and Leu455 (**Fig 1E**). Furthermore, the standard deviation of backbone RMSD around residues Leu455-Pro491 and the N-terminal of RBD (Thr333-Thr345) among the four repeated MD trajectories were approximately 2Å, indicating significant conformational change in the region. RMSF calculations of main-chain atoms showed significant atomic fluctuations (≥1.5 Å) for Lys458, Asn460, Lys462, Arg466, Ser477 and Asn481 upon binding to the ligand pixatimod. These results indicate that a conformational change may be induced by binding of pixatimod to S1 RBD (**Fig 1C**).

An alternate heparin binding site is reported around residues Arg403, Arg406, Arg408, Gln409, Lys417, Gln493, Gln498 (*8*). One of the replicates indicated a second binding mode wherein the tetrasaccharide of pixatimod was found to interact around this region (Supplementary Materials, **Fig S1**), however, the free energy of binding was > +13 kcal/mol indicating much less favourable binding to this site. Overall, our modelling data strongly support the notion of direct binding of pixatimod to S1 RBD, potentially resulting in induction of a conformational change and interference with binding to ACE2.

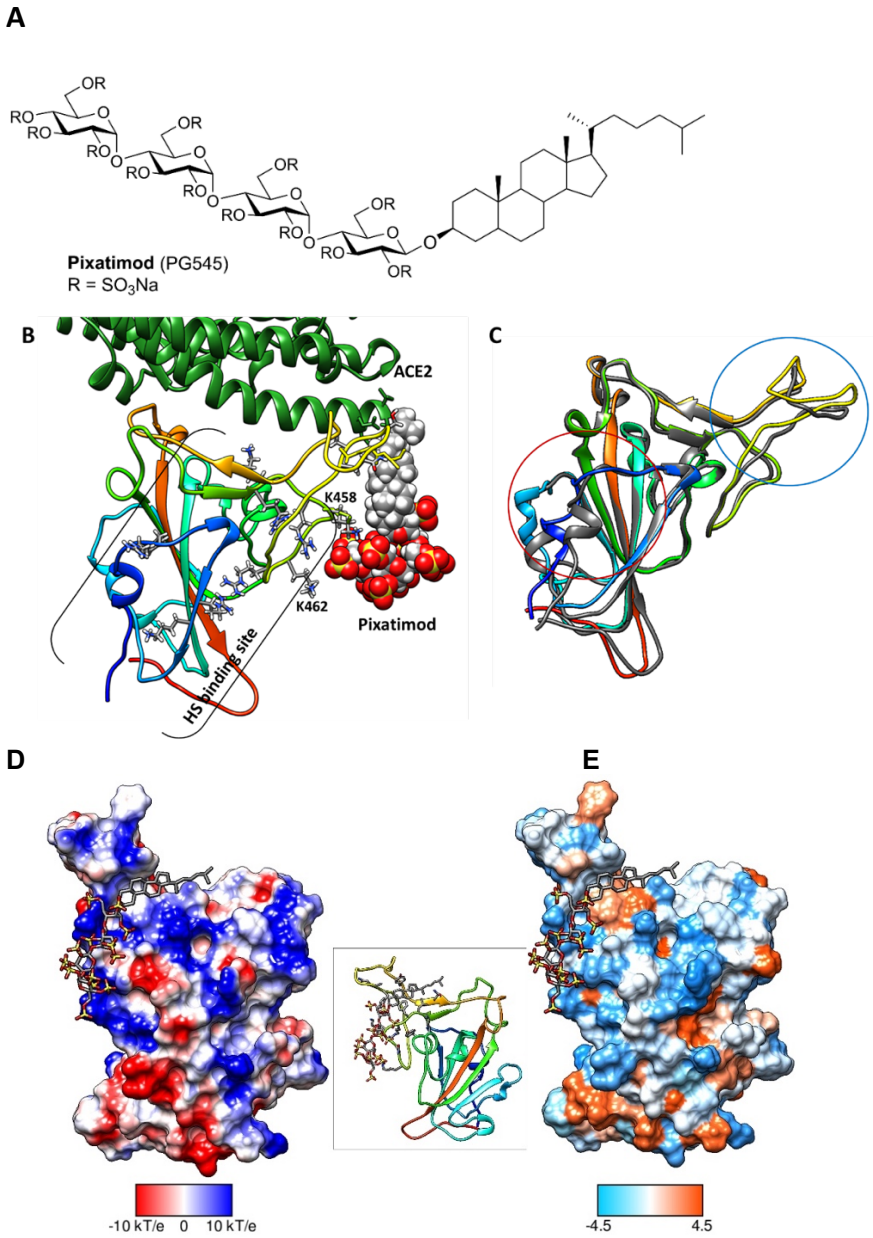

Figure 1: Molecular dynamics modelling defines direct interactions of pixatimod with S1 RBD: A, Structure of pixatimod. B, Model showing interactions of pixatimod with the RBD domain of spike protein. The sulfated tetrasaccharide partially occupies the HS/heparin binding site. The lipophilic tail of pixatimod wraps around the hydrophobic loop, thereby creating a steric clash with the helix of ACE2 protein (shown in inset-green ribbon). C, Superimposition of the X-ray structure (PDB: 6LZG) and one of the snapshots from MD simulations (ligand not shown) suggest conformational change around the loop region (blue circle) and the N-terminal helix as highlighted (red circle). D, columbic surface and E, hydrophobic surface binding mode of pixatimod to S1 RBD. Both surfaces are oriented in the same direction as shown in the ribbon diagram of the protein in the middle. The sulfated tetrasaccharide interacts with the basic regions on S1 RBD whereas cholestanol residue prefers hydrophobic region for interactions. Coulombic surface coloring defaults: $\varepsilon = 4r$, thresholds $\pm$ 10 kcal/mol were used. Blue indicates surface with basic region whereas red indicates negatively charged surface. The hydrophobic surface was colored using the Kyte-Doolittle scale wherein blue, white and orange red colour indicates most hydrophilicity, neutral and hydrophobic region, respectively. UCSF Chimera was used for creating surfaces and rendering the images. Hydrogens are not shown for clarity.

175 **Pixatimod interacts with spike protein**

176 Spectroscopic studies with circular dichroism (CD) allow investigation of direct binding of
177 compounds to recombinant spike protein receptor binding domain (S1 RBD), the region which
178 interacts with the ACE2 receptor on human cells. CD spectroscopy in the far UV region (λ = 190 -
179 260 nm) detects conformational changes in protein secondary structure that occur in solution and
180 can infer binding by an added ligand. Such secondary structural changes can be quantified using
181 spectral deconvolution. SARS-CoV-2 EcS1-RBD underwent conformational change in the
182 presence of either pixatimod or heparin as a comparator sulfated molecule known to bind the RBD
183 (*6-10*), consisting of decreased α-helical content for pixatimod and increased α-helical content for
184 heparin (**Fig 2C**). A decrease in global β-sheet content is observed for both pixatimod and heparin,
185 along with increases in turn structure (**Fig 2C**).
186

187 We explored the effects of pixatimod on protein stability using differential scanning fluorimetry
188 (DSF) in which the thermal denaturation of a protein is monitored in the presence of a hydrophobic
189 fluorescent dye (*20*). Binding of pixatimod induced a notably large reduction in melting temperature
190 (ΔT_m) of 9.1ºC (**Fig 2D**; p=0.0001), indicating major destabilisation of the mammalian expressed
191 S1-RBD (mS1 RBD) protein. In contrast, heparin at an equivalent dose only partially destabilised
192 the RBD protein, evidenced by a small side peak shifted by ~5-6 ºC indicating populations of RBD
193 in a bound and unbound state (**Fig 2D**).

194 The observed changes demonstrate that the SARS-CoV-2 S1 RBD interacts with pixatimod in
195 aqueous conditions of physiological relevance. Notably, the conformational changes and
196 destabilization observed were distinct for pixatimod compared to heparin, suggesting distinct
197 interactions (**Fig 2**). Consistent with the modelling results, these data confirm direct interactions of
198 pixatimod with S1 RBD, resulting in induction of a conformational change, consistent with the
199 notion that HS mimetics such as pixatimod have the potential to interfere with S1-RBD interactions
200 with ACE2.
201
202

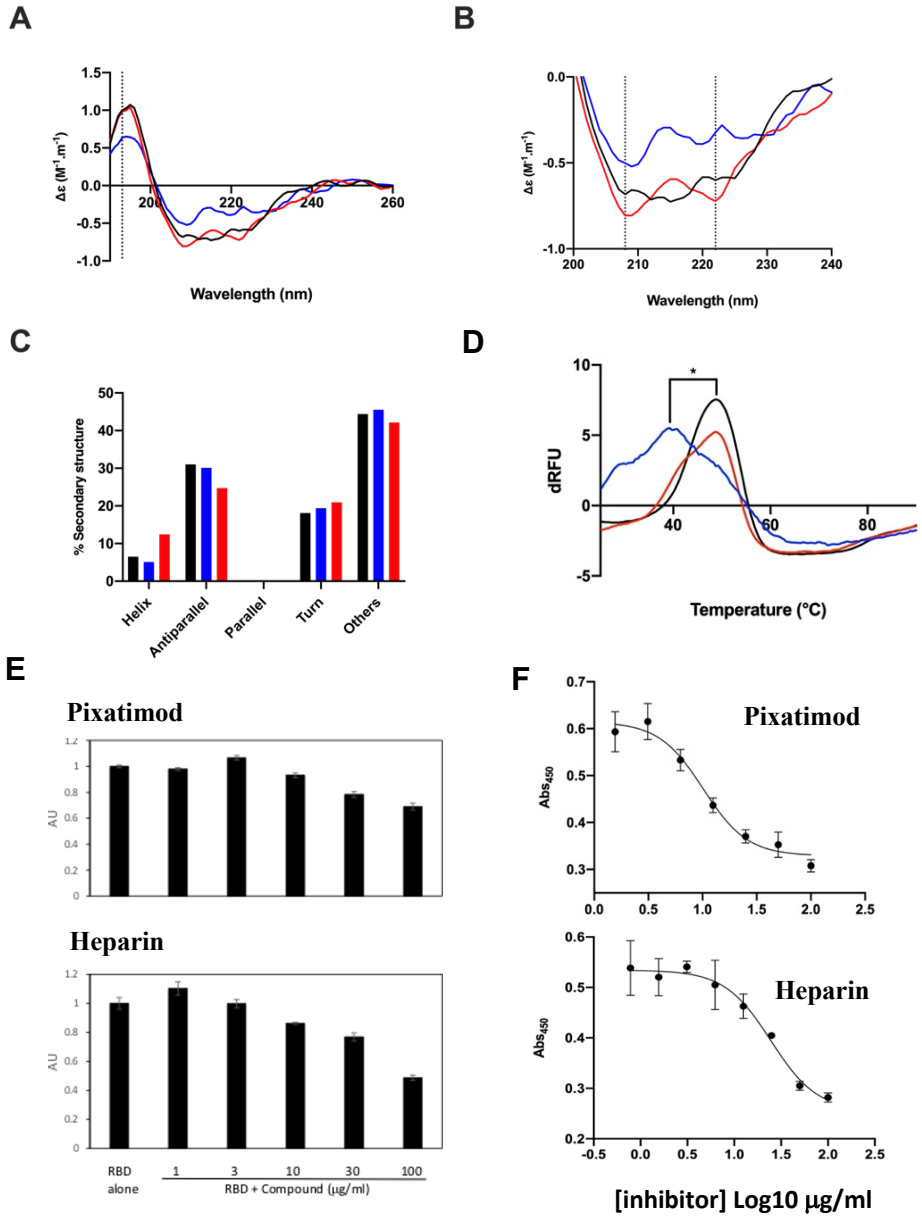

Figure 2: Pixatimod interacts with SARS-CoV-2 S1-RBD and inhibits binding to cells and ACE2 receptor. A, Circular dichroism spectra (190 - 260 nm) of SARS-CoV-2 EcS1-RBD alone (black), or with heparin (red) or pixatimod (blue). The vertical dotted line indicates 193 nm. **B,** The same spectra expanded between 200 and 240 nm. Vertical dotted lines indicate 222 nm and 208 nm. **C,** Secondary structure content analysed using BeStSel for SARS-CoV-2 EcS1-RBD. α-helical secondary structure is characterized by a positive band at ~193 nm and two negative bands at ~208 and ~222 nm (analysis using BeStSel was performed on smoothed data between 190 and 260 nm). **D,** Differential scanning fluorimetry of binding of pixatimod (blue; 10µg) or heparin (red; 10 µg) to mS1-RBD (1µg; black line, protein-only control). *T_m values for RBD alone (48.4 ºC, SD = 0.3) and in the presence of PG545 (39.3 ºC, SD = 1) were statistically different, $t(4) = 15.25$, $p = 0.0001$. **E**: dose response effects of pixatimod (E) and unfractionated porcine mucosal heparin (F) on binding of EcS1-RBD to Vero cells. Data were normalised to control with no addition of EcS1-RBD. AU, arbitrary units of fluorescence. n=3 +/- CV. **F,** Competitive ELISA assay using biotinylated human ACE2 protein immobilized on streptavidin coated plates, to measure inhibition of binding of mS1-RBD to in the presence of various concentrations of inhibitor compounds. Pixatimod (IC_{50}, 10.1 µg/ml) and porcine mucosal heparin (IC_{50}, 24.6 µg/ml). n=3, +/-SD; representative example shown.

237 **Pixatimod inhibits S1-RBD cell-binding**

238 We next evaluated inhibition of binding of His-tagged EcS1-RBD to monkey Vero cells (which are
239 known to express both HS proteoglycans (HSPGs) and the ACE2 protein receptor required for
240 SARS-CoV-2 attachment and cell invasion). Fixed cells were exposed to His-tagged S1 RBD for
241 1hr, in the presence or absence of additional compounds, with subsequent washing and detection
242 using a fluorescently-labelled anti-His tag antibody. A clear dose response was noted for both
243 pixatimod and heparin as a comparator compound (**Fig 2E**), with 32% and 51% inhibition achieved
244 at 100 µg/mL respectively. These data confirm that pixatimod can interfere with binding of S1-
245 RBD to cells containing HSPGs and ACE2 protein receptors.

246

247

248 **Pixatimod inhibits S1-RBD binding to ACE2**

249 To further evaluate the mechanism of action of pixatimod its direct effects on the interaction of S1-
250 RBD with the ACE2 protein receptor was measured using a competitive ELISA assay. Inhibition
251 of binding of mS1-RBD preincubated with various concentrations of inhibitor compounds was
252 measured by detection with an anti-RBD antibody. A dose response was observed with pixatimod
253 showing an IC_{50} of 10.1 µg/ml (**Fig 2F**). In comparison heparin also demonstrated inhibitory
254 activity but with lower potency (24.6 µg/ml; **Fig 2F**). Importantly, this data confirms a direct
255 mechanism of action of pixatimod via inhibition of S1-RBD binding to the ACE2 protein receptor.

256

257 **Pixatimod inhibits SARS-CoV-2 infection**

258 The effect of pixatimod on SARS-CoV-2 infection of Vero cells was examined using a standard
259 plaque reduction neutralisation assay. Pixatimod was pre-incubated with the SARS-CoV-2 clinical
260 isolate from Victoria, Australia (VIC01) for 1 hr before infecting the cells. Significant decreases
261 were observed in the number of PFU upon pixatimod treatment for SARS-CoV-2 **(Fig 3A**).
262 Analysis of multiple dose response curves yielded an EC_{50} for pixatimod in the range of 2.4-13.8
263 µg/mL (mean 8.1 µg/ml; n=3 assays) (**Table 1**). In comparison, an EC_{50} of ~10 µg/ml has been
264 observed for unfractionated heparin with a SARS-CoV-2 Italy UniSR1/2020 isolate (*8*) and 20-64
265 µg/ml for the SARS-CoV-2 Victoria isolate (*21*).

266

267

268

269

270

271

A **B**

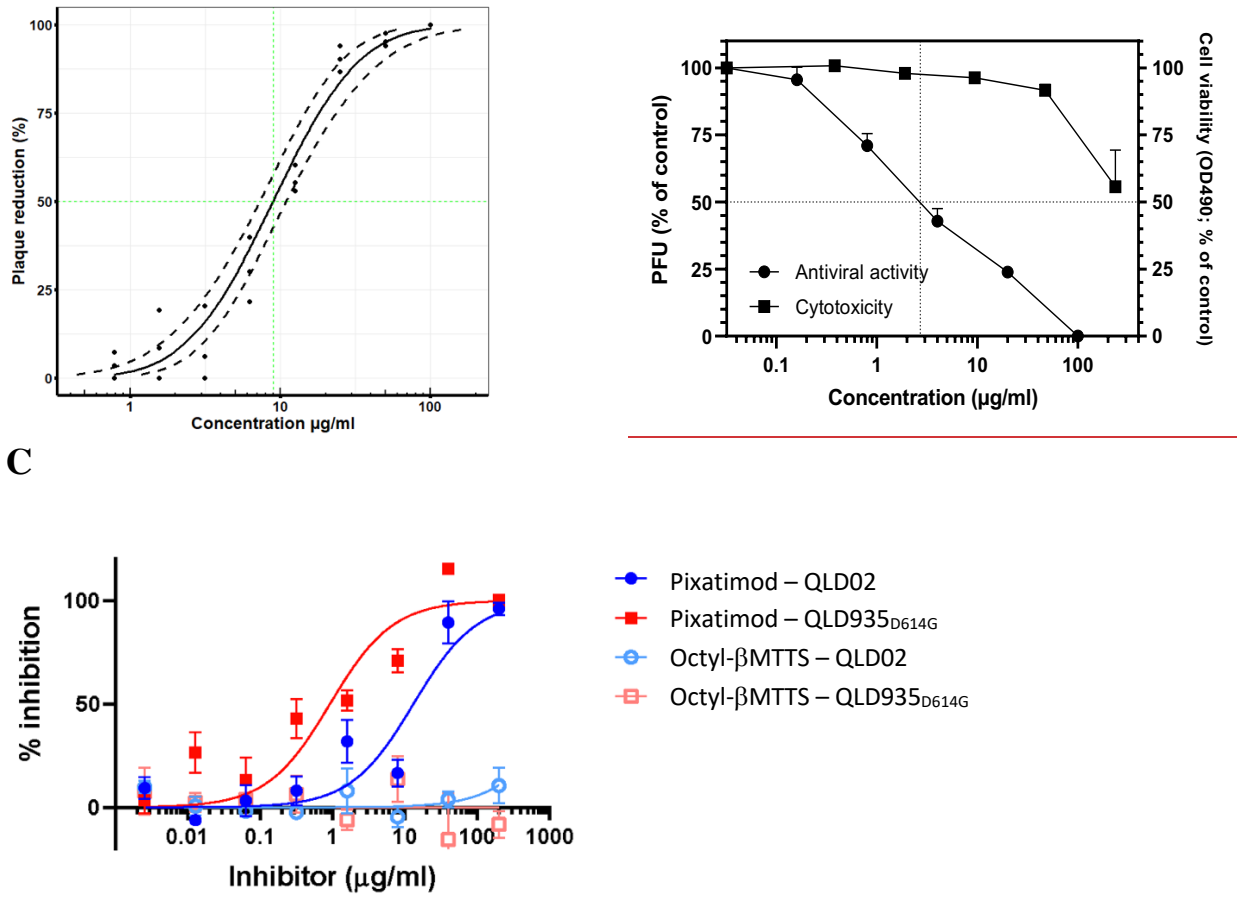

Figure 3: Pixatimod inhibits attachment and invasion of Vero cells by live SARS-CoV-2 virus isolates. Live virus infectivity assays were performed as described in Methods for 3 different SARS-CoV-2 isolates (representative data shown). A, Plaque reduction neutralization assay of Victoria isolate (VIC01) with a Probit mid-point analysis curve ±95% confidence intervals (dashed lines) (EC_{50} 8.9 µg/ml; 95% CI, 7-11; n=3). B, Plaque reduction assay of DE isolate, EC_{50} 2.7 µg/ml; n=3, +/- SD. C, Cytopathic assay of Queensland isolates, EC_{50} 13.2 (QLD02) and 0.9 (QLD935 with D614G mutation) µg/ml n=6, +/- SEM. Representative examples are shown in each case. Results of pixatimod inhibition of SARS-CoV-2 infectivity are expressed as percent plaque reduction (A), plaque number as a percent of control (B), or percent inhibition from cytopathic effect (C). Panel B also shows cytotoxicity data for Vero cells for calculation of CC_{50} value (>236 µg/ml). In panel C, data is also shown for octyl β-maltotetraoside tridecasulfate (Octyl-βMTTS; Supplementary Materials Fig S2), an analogue of pixatimod which lacks the steroid side-chain.

To establish that these antiviral effects were relevant for wider clinical viral isolates, assays were conducted with the isolate DE-Gbg20 from Sweden in a plaque reduction assay. Pixatimod inhibited infectivity of the DE-Gbg20 isolate with an EC_{50} value of 2.7 µg/mL (**Fig 3B**), similar to that found in experiments with the VIC01 isolate. Analysis of pixatimod cytotoxicity for Vero cells using a tetrazolium-based assay revealed that pixatimod decreased by 50% (CC_{50}) the viability of Vero cells at concentration >236 µg/mL, i.e., well above the EC_{50} values observed in the plaque reduction assay (**Fig. 3B; Table 1**). Selectivity index (SI) values for pixatimod ranged from >17 to >98 for these assays.

Table 1: Anti-SARS-CoV-2 activities of pixatimod in Vero cells.

SARS-CoV-2 isolate	Assay Method	EC_{50} (µg/mL)[a]	CC_{50} (µg/mL)	Selectivity Index[a]
Victoria isolate	Plaque reduction	8.1 ± 3.1 (2.4-13.8)[a]	>236[d]	29 (>17 to >98[a])
DE-Gbg20 isolate	Plaque reduction	2.7[b]		>87
	Cytopathic effect	(0.8 – 11.6[c])		>20 to >295
QLD02 isolate	Cytopathic effect	13.2 (8.0 – 21.6)		>17
QLD935 isolate	Cytopathic effect	0.9 (0.4 – 1.9)		>200

[a] Mean values and individual assay result ranges, and resulting selectivity index ranges, in brackets.
[b] Mean EC_{50} ±1SE based on the data from three independent virus plaque reduction assays ($PRNT_{50}$ values).
[c] EC_{50} computed by the Reed and Muench formula based on the cytopathic effect assay. Range indicates upper (complete protection of cells) and lower (partial protection) limits of EC_{50} estimation.
[d] Cytotoxicity in Vero cells (determined at University of Gothenburg).

In addition to the plaque reduction assays pixatimod inhibition of SARS-CoV-2 infectivity was assessed using assays that measured the cytopathic effects of the virus as an endpoint. Using the Swedish DE-Gbg20 isolate, and two Australian isolates from Queensland (QLD02 and QLD935), the EC_{50}s for pixatimod inhibition of SARS-CoV-2 infectivity were determined to be 0.8-11.6, 10.6 and 0.9 µg/mL, respectively (**Table 1**), values were comparable with those observed for the plaque reduction assays (**Table 1**). We also noted that a pixatimod analogue octyl β-maltotetraoside tridecasulfate (without the steroid side-chain) (**Fig S2**) lacked efficacy for both QLD02 and QLD935 isolates (**Fig 3C**), demonstrating the importance of the steroid side-chain for activity. Notably, both DE-Gbg20 and QLD935 isolates contain the D614G mutation of the spike protein commonly present in recent isolates (Table S1) (*22*). The QLD935 isolate exhibited lower cytopathicity, which could partially contribute to the observed lower EC_{50} for pixatimod against this isolate.

Discussion

The current COVID-19 pandemic illustrates the critical need to develop effective vaccines and therapeutics for emerging viruses and established antiviral agents appear to have limited utility against SARS-CoV-2. Owing to their use as a means of cell attachment by many viruses, HS represents an ideal broad-spectrum antiviral target (*2*). Binding of a viral protein to cell-surface HS is often the first step in a cascade of interactions that is required for viral entry and the initiation of infection (*23*). As HS and heparin contain the same saccharide building blocks and HS-binding proteins also interact with heparin, this drug is gaining attention (apart from its anticoagulant properties) in COVID-19 treatment (*23*). Here we demonstrate a direct mechanism of action of pixatimod and heparin on attenuating S1-RBD binding to ACE2. These data are supported by recent studies on heparin using native mass spectrometry (*24*), and also demonstrate the ability of HS mimetics to inhibit S1-RBD binding.

Heparin has been shown to inhibit binding of SARS-SoV-2 spike protein to a human cell line (*25*), and to inhibit entry into human cells of pseudovirus carrying the SARS-CoV-2 spike protein

(10,*26*). However, the question of whether therapeutic doses of heparins are effective for COVID-19 patients as an antiviral treatment awaits the outcome of clinical trials; bleeding complications are possible (*27*), though non-anticoagulant heparin or HS preparations could be deployed that reduce cell binding and infectivity without a risk of causing bleeding (*9,10*). However, HS mimetics offer additional advantages in comparison to heparin beyond simply reducing anticoagulant activity (9), most notably their ready availability at scale via synthetic chemistry production that addresses the well-known fragility of the heparin supply chain (*11*). As a clinical-stage HS mimetic, pixatimod provides better control over structure, molecular weight diversity (a single molecular entity), sulfation, purity and stability. Herein, we reveal a direct interaction of the clinical candidate pixatimod with the S1 spike protein RBD, supported by molecular modelling data. Pixatimod also inhibited the interaction of S1 RBD with Vero cells which express the ACE2 receptor. Moreover, infectivity assays, of two types (plaque reduction and cytopathic effect, Table 1) confirm pixatimod is a potent inhibitor of SARS-CoV-2 infection of Vero cells, at concentrations ranging from 0.8 to 13.8 µg/mL which are well within its known therapeutic range. Interestingly, we noted that the lipophilic steroid side chain of pixatimod was critical for its potency and is predicted from modelling to interact with S1-RBD. This unique feature, making it an unusual amphiphilic HS mimetic, has also been shown to confer virucidal activity against Herpes Simplex virus by disruption of the viral lipid envelope (*15*).

Pixatimod has only mild anti-coagulant activity, and has been administered i.v. to over 80 cancer patients, being well tolerated with predictable pharmacokinetics (PK) and no reports of heparin-induced thrombocytopenia (*12*). Further, cytotoxicity *in vitro* is low; we observed a CC_{50} >100 µM (>236 µg/mL) in Vero cells, consistent with cytotoxicity data on human cells (*28*). Importantly, the maximum plasma concentration (Cmax) of pixatimod following a single treatment of 100 mg in cancer patients is 29.5 µg/mL with a Cmin of 2.7 µg/mL measured one week following treatment (*12*), indicating that an equivalent dosing regimen should be sufficient to achieve antiviral activity in human subjects. The low anticoagulant activity of pixatimod is an advantage since it could be used as a direct antiviral agent in combination therapies with heparin, which are being used to treat coagulopathies observed in COVID-19 patients (*29*). It was also encouraging that pixatimod inhibition of multiple clinical isolates of SARS-CoV-2 was noted, demonstrating potential for widespread effectiveness. Presence of multiple binding sites for pixatimod in the Spike protein would suggest robustness against mutations that may arise later in pandemic and/or in the following coronavirus outbreaks. While recent widespread isolates with D614G spike mutants appear to be 2-3 fold more sensitive to the antiviral activity of pixatimod, caution needs to be taken in interpreting the data of the cytopathicity assay used to determine this activity as 614G isolates (at least QLD935) exhibited lower cytopathicity than 614D isolates.

It is notable that there are multiple potential mechanisms of action of pixatimod against SARS-CoV-2 (summarised in **Fig 4**), including direct inhibition of HS-S1-ACE2 interactions but also immunomodulatory effects which may alleviate some of the immunopathologies associated with moderate-severe COVID-19 patients. Pixatimod also inhibits the pro-inflammatory enzyme heparanase (*28*) and has been demonstrated to suppress IL-6 in inflammatory (pancreatitis) and viral (Ross River virus) animal models (*14, 18*). Moreover, it blocks the heparanase-dependent invasion of macrophages into tumours in mouse cancer models (*29*) which may be relevant to

invasion of monocytes and macrophages into the lungs associated with severe COVID-19 disease (*30*), representing an immunopathology potentially responsive to agents such as pixatimod. Vaccinia virus has recently been shown to rely on host heparanase to degrade HS in order to spread to distant sites (*31*), revealing a role for heparanase in the progression of disease that may also apply for SARS-CoV2 in COVID-19. Notably, increased plasma heparanase activity is associated with COVID-19 (*32*). Thus additional beneficial effects of pixatimod might be anticipated from its heparanase inhibitory properties.

Based on the data presented here, pixatimod has potent antiviral activity against SARS-CoV-2 at therapeutically relevant concentrations in addition to its known heparanase-inhibitory and immunomodulatory properties which may further support the host response to COVID-19 infection. Collectively this provides a strong rationale to justify entry of pixatimod to clinical trials for COVID-19.

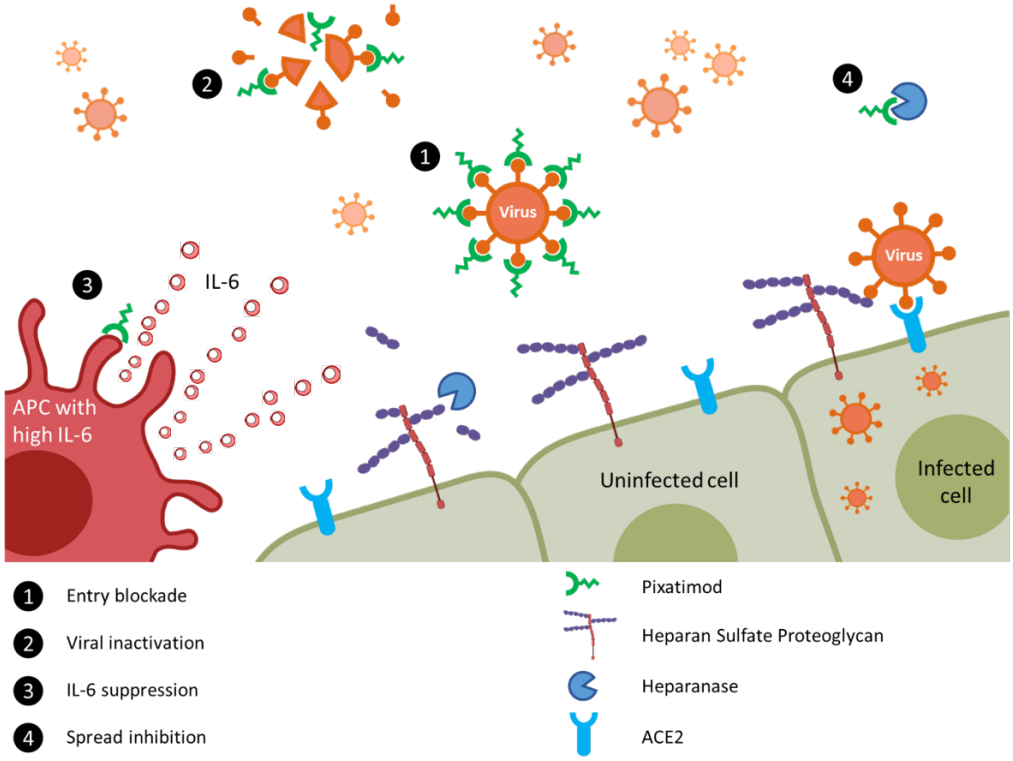

Figure 4: Proposed multi-mode mechanisms of pixatimod activity against SARS-CoV-2 and other viruses. The principal mode of action demonstrated here is that pixatimod acts as a decoy receptor [1], blocking S1-RBD binding to HS co-receptors and inhibiting viral attachment to host cells, thus blocking viral infection. Additional potential modes of action include: [2] virucidal activity of pixatimod, dependent upon the cholestanol moiety (*15*), which may lead to degradation and permanent inactivation of SARS-CoV-2 virus particles; [3] suppression of IL-6 secretion by antigen presenting cells, primarily macrophages (*14*); and [4] blocking viral escape from host cell by inhibiting heparanase which otherwise promotes viral escape by cleaving HS receptors (*31, 32*).

Materials and Methods

Computational methods: The crystal structure of the RBD-ACE2 complex (PDB ID: 6LZG, Wang et al, 2020) was retrieved from the RCSB Protein Data Bank. Structures were stripped of water molecules, ACE2 chain and any cofactors and/or ligands present. UCSF Chimera was used to edit the structure and for visualisation. Without prior knowledge of the pixatimod binding site, one molecule of the ligand was placed in the simulation system containing the protein, solvent and ions and molecular dynamics (MD) simulations were performed for 600 ns using the AMBER16 package. Such unguided simulations, as reviewed before (*33*), have been used to predict the binding sites on a protein's surface and drive the design of new ligands. All the MD simulations were carried out using the pmemd.cuda module (*34*) of the AMBER 16 molecular dynamics package and the analyses were performed using the cpptraj module of AmberTools16 (*35*). Simulation systems were set up by placing the spike RBD domain at the centre of the octahedral simulation box (with an extension of at least 12 Å from each side). Pixatimod was randomly placed in the box. This was followed by addition of TIP3P water (*36*) and Na^+ ions for neutralising the charge of the system. Proteins were parameterized using the Amber99SB-ildn force field (*37*) whereas Glycam-06 (version j) (*38*) and Lipid14 (*39*) force fields were used for the sulfated tetrasaccharide and cholestanol moieties of pixatimod, respectively. Four replicates of the unguided simulations were performed (4 × 600 ns). Periodic boundary conditions were applied, and the time step was set to 2 fs. The electrostatic energy was calculated with the particle mesh Ewald (PME) method. SHAKE constraints were applied on the bonds involving hydrogen. A cut-off of 12 Å was applied to the Lennard-Jones and direct space electrostatic interactions with a uniform density approximation included to correct for the long-range van der Waals interactions.

The system was first minimized without electrostatics for 500 steps, then with a restraint of 25 kcal/(mol $Å^2$) applied on the protein and pixatimod. This minimization was followed by 100-ps MD simulation with 25 kcal/(mol $Å^2$) positional restraints applied on the protein and ligand, and the temperature was slowly increased from 0 to 300 K. Then, followed by 500 steps of steepest descent cycles followed by 500 steps of conjugate gradient minimization, and 50-ps equilibrations with a restraint force constant of 5 kcal/(mol $Å^2$) in the protein and ligand, followed by final 2 ns equilibration without restraints to equilibrate the density. The first few steps were all carried out at constant volume followed by at least 600 ns production MD simulation at 300 K (Langevin dynamics, collision frequency: 5/ps) with 1-atm constant pressure. Trajectories were collected and data analyses such as RMSD, RMSF and free energy of binding were performed on the last 30000 frames. The binding free energy and pairwise residue contributions (*40*) were calculated using the Molecular mechanics-Generalized Born (GB) equation (MM/GBSA) procedure implemented in AmberTools16. The details of this method have been extensively reviewed (*41*). The polar solvation energy contribution was calculated by using $GB^{OBC\ II}$ (igb= 5) (*42*). The value of the implicit solvent dielectric constant and the solute dielectric constant for GB calculations was set to 80 and 1, respectively. The solvent probe radius was set to 1.4 Å as default. The entropy calculation is computationally expensive and therefore not performed for the purposes of this study.

Expression of His-tagged recombinant SARS-CoV-2 S1 RBD in E coli: Residues 330−583 of the SARS-CoV-2 spike protein (GenBank: MN908947) were cloned upstream of a N-terminal

450 6XHisTag in the pRSETA expression vector and transformed into SHuffle® T7 Express Competent
451 *E. coli* (NEB, UK). Protein expression was carried out in MagicMediaTM *E. coli* Expression Media
452 (Invitrogen, UK) at 30°C for 24 hrs, 250 rpm. The bacterial pellet was suspended in 5 mL lysis
453 buffer (BugBuster Protein Extraction Reagent, Merck Millipore, UK; containing DNAse) and
454 incubated at room temperature for 30 mins. Protein was purified from inclusion bodies using IMAC
455 chromatography under denaturing conditions. On-column protein refolding was performed by
456 applying a gradient with decreasing concentrations of the denaturing agent (from 8M Urea). After
457 extensive washing, protein was eluted using 20 mM NaH_2PO_4, pH 8.0, 300 mM NaCl, 500 mM
458 imidazole. Fractions were pooled and buffer-exchanged to phosphate-buffered saline (PBS; 140
459 mM NaCl, 5 mM NaH_2PO_4, 5 mM Na_2HPO_4, pH 7.4; Lonza, UK) using Sephadex G-25 media (GE
460 Healthcare, UK). Recombinant protein (termed EcS1-RBD) was stored at -4°C until required.

461 ***Expression of S1-RBD in mammalian cells:*** Secreted RBD-SD1 (termed mS1-RBD) was
462 transiently produced in suspension HEK293-6E cells. A plasmid encoding RBD-SD1, residues
463 319−591 of 2019-nCoV S were cloned upstream of a C-terminal HRV3C protease cleavage site, a
464 monomeric Fc tag and an His_{8x} Tag were a gift from Jason S. McLellan, University of Texas at
465 Austin. Briefly, 100 mL of HEK293-6E cells were seeded at a cell density of 0.5 × 106 cells/ml
466 24hr before transfection with polyethyleneimine (PEI). For transfection, 100 µg of the ACE2
467 plasmid and 300 µg of PEI (1:3 ratio) were incubated for 15 min at room temperature. Transfected
468 cells were cultured for 48 hr and fed with 100 mL fresh media for additional 48 hr before harvest.
469 RBD-SD1was purified by HiTrap Protein G HP column (GE Healthcare, US) pre-equilibrated in
470 PBS and eluted with 0.1M glycine (pH 2.7). Purity of proteins was evaluated by Coomassie staining
471 of SDS-PAGE gels, and proteins were quantified by BCA Protein Assay Kit (Thermo Scientific).

472 ***Secondary structure determination of SARS-CoV-2 S1 RBD by circular dichroism spectroscopy:***
473 The circular dichroism (CD) spectrum of the SARS-CoV-2 S1 RBD in PBS was recorded using a
474 J-1500 Jasco CD spectrometer (Jasco, UK), Spectral Manager II software (JASCO, UK) using a
475 0.2 mm path length, quartz cuvette (Hellma, USA). All spectra were obtained using a scanning of
476 100 nm/min, with 1 nm resolution throughout the range λ = 190 - 260 nm and are presented as the
477 the mean of five independent scans, following instrument calibration with camphorsulfonic acid.
478 SARS-CoV-2 S1 RBD was buffer-exchanged (prior to spectral analysis) using a 10 kDa Vivaspin
479 centrifugal filter (Sartorius, Germany) at 12,000 g, thrice and CD spectra were collected using 21
480 µL of a 0.6 mg/mL solution in PBS, pH 7.4. Spectra of heparin (unfractionated porcine mucosal
481 heparin, Celsus) were collected in the same buffer at approximately comparable concentrations,
482 since this is a polydisperse material. Collected data were analysed with Spectral Manager II
483 software prior to processing with GraphPad Prism 7, using second order polynomial smoothing
484 through 21 neighbours. Secondary structural prediction was calculated using the BeStSel analysis
485 server (*43*).

486 To ensure that the CD spectral change of SARS-CoV-2 S1 RBD in the presence of pixatimod did
487 not arise from the addition of the compound alone, a difference spectrum was analysed. The
488 theoretical CD spectrum that resulted from the arithmetic addition of the CD spectrum of the SARS-
489 CoV-2 S1 RBD and that of pixatimod differed from the observed experimental CD spectrum of
490 SARS-CoV-2 S1 RBD mixed with compound alone. This demonstrates that the change in the CD

491 spectrum arose from a conformational change following binding to pixatimod (Supplementary
492 Materials, Fig S3).

493 ***Differential scanning fluorimetry:*** Differential scanning fluorimetry (DSF) was conducted on
494 mammalian expressed mS1-RBD (1 µg) in PBS pH 7.6 and 1.25 X Sypro Orange (Invitrogen) to
495 a total well volume of 40 µL in 96-well qPCR plates (AB Biosystems). Unfractionated porcine
496 mucosal Heparin (Celsus) or pixatimod (10 µg) were introduced to determine the effect on the
497 thermal stability of, mS1-RBD using an AB biosystems StepOne plus qPCR machine, employing
498 the TAMRA filter setting. Melt curve experiments were performed following a 2-minute initial
499 incubation at 25 °C, with succeeding 0.5 °C increments every 30 s up to a final temperature of
500 90°C. Control wells containing H_2O, heparin or pixatimod (10 µg) without mS1-RBD (1µg) also
501 employed to ensure a change in the melt curve was solely a result of protein-ligand interactions and
502 interactions with Sypro Orange. Smoothed first derivative plots (9 neighbours, 2nd-order
503 polynomial, Savitxky-Golay) were constructed using Prism 8 (GraphPad). T_m values were
504 calculated using MatLab softaware (R20018a, MathWorks) and ΔT_m values determined from the
505 difference between the T_m of RBD alone or in the presence of heparin or pixatimod.

506 ***Cell binding of S1 RBD:*** African green monkey Vero kidney epithelial cells (Vero E6) were
507 purchased from ATCC. Cells were maintained at 50-75% confluence in DMEM supplemented
508 with 10% foetal bovine serum, 20 mM L-glutamine, 100 U/mL penicillin-G and 100 U/mL
509 streptomycin sulfate (all purchased from Gibco/ThermoFisher, UK). Cells were maintained at 37
510 ºC, in 5% CO_2 and plated into 96-well cell culture plates at 1000 cells/well in 100 µL of
511 maintenance medium. Cells were allowed to adhere overnight. Medium was aspirated and wells
512 were washed 3x with 200 µL calcium, magnesium-free PBS (CMF-PBS, Lonza, UK). Cells were
513 fixed with 100 µL 10% neutral buffered Formalin (Thermofisher, UK) for 10 minutes at room
514 temperature, then washed 3x with 200 µL CMF-PBS. 100 µL CMF-PBS was added to each well
515 and plates were stored at 4 °C until use. Before use, wells were blocked with 200 µL CMF-PBS +
516 1% BSA (Sigma-Roche, UK) for 1 hour at room temperature, and washed 3x with 200 µL CMF-
517 PBS + 0.1% Tween-20 (PBST, Sigma-Roche, UK) followed by 2x with 200 µL CMF-PBS.
518 His-tagged S1-RBD (50 µg/mL) and compounds at indicated concentrations were added to each
519 well in 25 µL PBST + 0.1% BSA as indicated. Wells were incubated for 1 hour at room temperature
520 with rocking. Wells were washed 3x with 200 µL PBST and 2x with 200 µL CMF-PBS. Binding
521 of His-tagged S1-RBD was detected with Alexa Fluor 488 anti-his tag antibody (clone J095G46,
522 Biolegend, UK) 1:5000 in 25 µL PBST + 0.1% BSA per well. Wells were incubated in the dark
523 for 1 hour at room temperature with rocking. Wells were washed 3x with 200 µL PBST and 2x
524 with 200 µL CMF-PBS. Fluorescence was read at Ex. 485:Em 535 on a Tecan Infinite M200Pro
525 plate reader. Results are presented as normalized mean (where 0 is the fluorescence without added
526 S1-RBD, and 1 is the fluorescence with 50 µg/mL S1-RBD; ± %CV, n=3).
527

528 ***Competition ELISA for S1 RBD binding to ACE2:*** High binding 96 well plates (Greiner) were
529 coated with 3 µg/mL streptavidin (Fisher) in 50 mM sodium carbonate buffer pH 9.6 (50 µL/ well)
530 for 1 hour at 37 ºC. Plates were washed 3 times with 300 µL PBS, 0.2% Brij35 (PBSB) and blocked
531 with 300 µL PBSB + 1% casein for 1 hour at 37 ºC. Plates were washed a further 3 times with 300

532 µL PBSB prior to the addition of 100 ng/mL BiotinylatedACE2 (Sino Biological) in PBSB + 1%
533 casein (50 µL/ well) and incubated for 1 hour at 37 ºC. Plates were again washed 3 times with 300
534 µL PBSB prior to the addition of 50 µL/well mS1-RBD (5µg/mL) in PBSB + 1% casein, which had
535 been pre-incubated for 30 minutes at room temperature with or without varying concentrations of
536 heparin or pixatimod (100- 0.7 µg/mL) in separate tubes. Plates were incubated for 1 hour at 37 ºC
537 to allow for mS1-RBD-ACE2 binding and were subsequently washed with 300 µL/well PBSB.
538 Bound mS1-RBD was detected by incubation with 0.5 µg/mL Rabbit-SARS-CoV-2 (2019-nCoV)
539 Spike RBD Antibody (Stratech) in PBSB + 1% casein (50 µL/well) for 1 hour at 37 ºC. Following
540 a further 3 washes with PBSB plates were incubated for 30 minutes at 37 ºC with horseradish
541 peroxidase conjugated Donkey anti-Rabbit IgG diluted 1:1000, v/v in PBSB + 1% casein
542 (Bioledgend). Plates were washed a final 5 times with 300 µL PBSB before being developed for 10
543 minutes with 3,3',5,5'- tetramethylbenzidine prepared according to the manufacturer's instructions
544 (Fisher). Reactions were stopped by the addition of 20 µL 2M H_sSO_4 and plates were read at λ =450
545 nm using a Tecan Infinate M200 Pro mulit-well plate reader (Tecan Group). Control wells
546 containing no biotinylated ACE2 were employed to ensure binding was specific.
547
548 ***Live SARS-CoV-2 virus assays:***
549 SARS-CoV-2 Victoria isolate (GISAID accession, EPI_ISL_406844): a plaque reduction assay was
550 performed with the SARS-CoV-2 Victoria/01/2020 (passage 3) isolate, generously provided by The
551 Doherty Institute, Melbourne, Australia at P1, was diluted to a concentration of 1.4 x 10^3 pfu/mL
552 (70 pfu/50µL) in minimal essential media (MEM) (Life Technologies, California, USA) containing
553 1% (v/v) foetal calf serum (FCS) (Life Technologies) and 25 mM HEPES buffer (Sigma) and mixed
554 50:50 with pixatimod dilutions, in a 96-well V-bottomed plate. The plate was incubated at 37 °C in
555 a humidified box for 1 hour to allow the virus to be exposed to pixatimod. The virus-compound
556 mixture was transferred onto the wells of a washed 24-well plate that had been seeded with Vero
557 E6 cells [ECACC 85020206] the previous day at 1.5 x 10^5 cells/well. The virus-compound mixture
558 was left to adsorb for an hour at 37°C, then plaque assay overlay media was applied (MEM
559 containing 1.5% carboxymethylcellulose (Sigma, Dorset, UK), 4% (v/v) FCS and 25 mM HEPES
560 buffer). After incubation at 37 °C in a humidified box, for 5 days, plates were fixed overnight with
561 20% (v/v) formalin/PBS, washed with tap water and then stained with methyl crystal violet solution
562 (0.2% v/v) (Sigma) and plaques were counted. Compound dilutions were performed in either
563 duplicate or quadruplicate. Compound dilutions and cells only were run in duplicate, to determine
564 if there was any cell cytotoxicity. A mid-point probit analysis (written in R programming language
565 for statistical computing and graphics) was used to determine the amount (µg/mL) required to
566 reduce SARS-CoV-2 viral plaques by 50% (PRNT50) compared with the virus only control
567 (n=5). An internal positive control for the PRNT assay was run in triplicate using a sample of heat-
568 inactivated human MERS convalescent serum known to neutralise SARS-CoV-2 (National Institute
569 for Biological Standards and Control, UK).
570
571 SARS-CoV-2 DE-Gbg20 isolate (GISAID accession under application): Plaque reduction assay
572 for SARS-CoV-2 clinical isolate DE-Gbg20 from Sweden was performed in a similar manner,
573 except for the virus and the pixatimod (fivefold decreasing concentrations at a range 100-0.16
574 µg/ml) were diluted in DMEM supplemented with 2% heat-inactivated FCS, and 100 U of penicillin
575 and 60 µg/ml of streptomycin (DMEM-S). The virus (100 PFU) and pixatimod (fivefold decreasing

concentrations at a range 100 – 0.16 µg/ml) were mixed and incubated for 30 min in humidified atmosphere comprising 5% CO_2 (CO_2 incubator). The mixtures were then transferred to Vero cells (ATCC CCL-81) and following incubation with cells for 90 min in the CO_2 incubator, the methylcellulose overlay was added. Three separate experiments each with duplicates were performed.

A cytopathic effect assay was performed with the SARS-CoV-2 DE-Gbg20 isolate and Vero cells (ATCC) plated at 2 x 10^4 per well in 96-well plates the day prior to the experiment. Serial fivefold dilutions of pixatimod in DMEM supplemented with 2% heat-inactivated FCS, and 100 U of penicillin and 60 µg/mL of streptomycin (DMEM-S) were incubated with 100 TCID50 of SARS-CoV-2 isolate DE for 20 min in humidified atmosphere comprising 5% CO_2 (CO_2 incubator). The final concentrations of pixatimod were in a range 0.075 µg/mL to 47.2 µg/mL. The cells were rinsed once with 50 µL of DMEM-S, and then 200 µL of the virus-pixatimod mixtures were added to each well with cells (in quadruplicates). After incubation of the virus-pixatimod mixtures with cells for 3 days in the CO_2 incubator, the cells were inspected under a microscope for the presence of virus induced cytopathic effect where complete protection of cells were denoted as "+" while a partial protection (~50% of cells showing no cytopathic effect) was recorded as "+/-". The 50% end-point (EC_{50}) was computed by the Reed and Muench method.

SARS-CoV-2 QLD02 (GISAID accession EPI_ISL_407896) and QLD935 (GISAID accession EPI_ISL_436097) clinical isolates from Australia: A cytopathic effect assay was carried out as described above for the DE-Gbg20 isolate, with 10 ffu/well and 3 days incubation. In this assay, Vero E6 cells were plated at 2 x 10^4 per well in 96-well plates the day prior to experiment. Serial five-fold dilutions of pixatimod in DMEM supplemented with 2% heat-inactivated FCS, and 100 U of penicillin and 60 µg/mL of streptomycin (DMEM-S) were incubated with 10 foci forming units of SARS-CoV-2 QLD02 or QLD935 isolate and incubated for 30 min in humidified atmosphere comprising 5% CO_2 (CO_2 incubator). The cells were rinsed once with 50 µL of DMEM-S, and then 200 µL of the virus-pixatimod mixtures were added to each well with cells (in triplicates). After incubation of the virus-pixatimod mixtures with cells for 3 days in the CO_2 incubator, the cells were fixed with 4% PFA and then stained with crystal violet. Then crystal violet was released by methanol and OD at 595nm was measured to quantify cell viability (protection from infection). The EC50 was then calculated using GraphPad Prism.

Cytotoxicity assays: The assay was performed as described by Lundin *et al*. (2012). Briefly, Vero cells (ATCC, 2 x 10^4 cells/well) were seeded in 96 well cluster plates to become nearly confluent at the day of the experiment. The cell growth medium was then removed and 100 µL of serial fivefold dilutions of pixatimod in DMEM-S (ranging from 0.09 to 236 µg/mL) were added to cells. Following incubation of cells with pixatimod for 3 days in the CO_2 incubator, 20 µL of the MTS salt containing CellTiter 96 Aqueous One Solution reagent (Promega, Madison, WI) was added and incubated for further 1-2 h at 37 °C. The absorbance was recorded at 490 nm against a background of 650 nm. Two separate experiments each in duplicates were performed and the results are expressed as percentage of absorbance value detected with pixatimod relative to control cells.

Statistical analysis: Experimental data are presented as means ± SD, SEM or CV as noted. Statistical analyses were performed using analysis of a two-tailed Student's *t* test with GraphPad

Prism (GraphPad Software) unless otherwise noted. Differences were considered statistically significant if the *P* value was less than 0.05.

References

1. Akhmerov, A., and Marbán, E. COVID-19 and the Heart. *Circ Res* 126**,** 1443-1455. (2020)
2. Cagno, V., Tseligka, E.D., Jones, S.T., and Tapparel, C. Heparan Sulfate Proteoglycans and Viral Attachment: True Receptors or Adaptation Bias? *Viruses* 11, 596.(2019)
3. Milewska, A., Zarebski, M., Nowak, P., Stozek, K., Potempa, J., and Pyrc, K. Human coronavirus NL63 utilizes heparan sulfate proteoglycans for attachment to target cells. *J Virol* 88**,** 13221-13230.(2014)
4. Vicenzi, E., Canducci, F., Pinna, D., Mancini, N., Carletti, S., Lazzarin, A., Bordignon, C., Poli, G., and Clementi, M. Coronaviridae and SARS-associated coronavirus strain HSR1. *Emerg Infect Dis* 10**,** 413-418.(2004)
5. Hoffmann, M., Kleine-Weber, H., Schroeder, S., Krüger, N., Herrler, T., Erichsen, S., Schiergens, T.S., Herrler, G., Wu, N.H., Nitsche, A., Müller, M.A., Drosten, C., and Pöhlmann, S. SARS-CoV-2 Cell Entry Depends on ACE2 and TMPRSS2 and Is Blocked by a Clinically Proven Protease Inhibitor. *Cell* 181**,** 271-280.e278.(2020)
6. Mycroft-West, C., Su, D., Elli, S., Guimond, S., Miller, G., Turnbull, J., Yates, E., Guerrini, M., Fernig, D., Lima, M., and Skidmore, M. The 2019 coronavirus (SARS-CoV-2) surface protein (Spike) S1 Receptor Binding Domain undergoes conformational change upon heparin binding. *bioRxiv***,** 2020.2002.2029.971093.(2020a)
7. Mycroft-West, C.J., Su, D., Li, Y., Guimond, S.E., Rudd, T.R., Elli, S., Miller, G., Nunes, Q.M., Procter, P., Bisio, A., Forsyth, N.R., Turnbull, J.E., Guerrini, M., Fernig, D.G., Yates, E.A., Lima, M.A., and Skidmore, M.A. SARS-CoV-2 Spike S1 Receptor Binding Domain undergoes Conformational Change upon Interaction with Low Molecular Weight Heparins. *bioRxiv***,** 2020.2004.2029.068486. (2020b)
8. Mycroft-West, C.J., Su, D., Pagani, I., Rudd, T.R., Elli, S., Guimond, S.E., Miller, G., Meneghetti, M.C.Z., Nader, H.B., Li, Y., Nunes, Q.M., Procter, P., Mancini, N., Clementi, M., Forsyth, N.R., Turnbull, J.E., Guerrini, M., Fernig, D.G., Vicenzi, E., Yates, E.A., Lima, M.A., and Skidmore, M.A. Heparin inhibits cellular invasion by SARS-CoV-2: structural dependence of the interaction of the surface protein (spike) S1 receptor binding domain with heparin. *Thrombosis and Haemostasis.* (in press) *bioRxiv***,** 2020.2004.2028.066761.(2020c)
9. Liu, L., Chopra, P., Li, X., Wolfert, M.A., Tompkins, S.M., and Boons, G.J. SARS-CoV-2 spike protein binds heparan sulfate in a length- and sequence-dependent manner. *bioRxiv*. doi.org/10.1101/2020.05.10.087288 (2020)
10. Clausen, T.M., Sandoval, D.R., Spliid, C.B., Pihl, J., Painter, C.D., Thacker, B.E., …..Esko, J.D. SARS-CoV-2 Infection Depends on Cellular Heparan Sulfate and ACE2. Cell, doi.org/10.1016/j.cell.2020.09.033 (2020)
11. Vilanova, E., Tovar, A.M.F., and Mourão, P.a.S. Imminent risk of a global shortage of heparin caused by the African Swine Fever afflicting the Chinese pig herd. *J Thromb Haemost* 17**,** 254-256.(2019)
12. Ferro, V., Liu, L., Johnstone, K.D., Wimmer, N., Karoli, T., Handley, P., Rowley, J., Dredge, K., Li, C.P., Hammond, E., Davis, K., Sarimaa, L., Harenberg, J., and Bytheway, I. Discovery of PG545: a highly potent and simultaneous inhibitor of angiogenesis, tumor growth, and metastasis. *J Med Chem* 55**,** 3804-3813.(2012)
13. Dredge, K., Brennan, T.V., Hammond, E., Lickliter, J.D., Lin, L., Bampton, D., Handley, P., Lankesheer, F., Morrish, G., Yang, Y., Brown, M.P., and Millward, M. A Phase I study of

the novel immunomodulatory agent PG545 (pixatimod) in subjects with advanced solid tumours. *Br J Cancer* 118**,** 1035-1041. (2018)

14. Khamaysi, I., Singh, P., Nasser, S., Awad, H., Chowers, Y., Sabo, E., Hammond, E., Gralnek, I., Minkov, I., Noseda, A., Ilan, N., Vlodavsky, I., and Abassi, Z. The Role of Heparanase in the Pathogenesis of Acute Pancreatitis: A Potential Therapeutic Target. *Sci Rep* 7**,** 715. (2017)

15. Said, J.S., Trybala, E., Görander, S., Ekblad, M., Liljeqvist, J., Jennische, E., Lange, S., and Bergström, T. The Cholestanol-Conjugated Sulfated Oligosaccharide PG545 Disrupts the Lipid Envelope of Herpes Simplex Virus Particles. *Antimicrob Agents Chemother* 60**,** 1049-1057.(2016)

16. Said, J., Trybala, E., Andersson, E., Johnstone, K., Liu, L., Wimmer, N., Ferro, V., and Bergström, T. Lipophile-conjugated sulfated oligosaccharides as novel microbicides against HIV-1. *Antiviral Res* 86**,** 286-295.(2010)

17. Lundin, A., Bergström, T., Andrighetti-Fröhner, C.R., Bendrioua, L., Ferro, V., and Trybala, E. Potent anti-respiratory syncytial virus activity of a cholestanol-sulfated tetrasaccharide conjugate. *Antiviral Res* 93**,** 101-109.(2012)

18. Supramaniam, A., Liu, X., Ferro, V., and Herrero, L.J. Prophylactic Antiheparanase Activity by PG545 Is Antiviral In Vitro and Protects against Ross River Virus Disease in Mice. *Antimicrob Agents Chemother* 62(4): e.01959-17 (2018)

19. Modhiran, N., Gandhi, N.S., Wimmer, N., Cheung, S., Stacey, K., Young, P.R., Ferro, V., and Watterson, D. Dual targeting of dengue virus virions and NS1 protein with the heparan sulfate mimic PG545. *Antiviral Res* 168**,** 121-127.(2019)

20. Uniewicz, K.A., Orio. A., Xu. R., Ahmed. Y., Wilkinson. M., Fernig. G. D and Yates. A. E. Differential Scanning Fluorimetry Measurements of Protein Stability Changes upon Binding to Glycosaminoglycans: A Screening Test for Binding Specificity. *Anal. Chem*. 82(9), 3796-3802 (2010)

21. Tree, JA., Turnbull, JE., Buttigieg, KR., Elmore, MJ., Coombes, N., Hogwood, J., Yates, EA., Gray, E., Singh, D., Wilkinson, T., Page, CP., Carroll, MW. Unfractionated heparin inhibits live wild-type SARS-CoV-2 cell infectivity at therapeutically relevant concentrations. *Authorea* DOI: 10.22541/au.159526747.71750127 (2020). *British J Pharmacol* (under revision)

22. Korber, B., Fischer, WM., Gnanakaran, S., Yoon, H., Theiler, J., Abfalterer, W., Hengartner, N., Giorgi, E.E., Bhattacharya, T., Foley, B., Hastie, K.M., Parker, MD., Partridge, DG., Evans, CM., Freeman, T.M., de Silva, TI., Sheffield COVID-19 Genomics Group., McDanal, C., Perez, L.G., Tang, H., Moon-Walker, A., Whelan, SP., LaBranche, CC., Saphire, EO. and Montefiori, D.C., Tracking Changes in SARS-CoV-2 Spike: Evidence that D614G Increases Infectivity of the COVID-19 Virus. *Cell.* 182: 812–827.e19. (2020)

23. Lindahl, U., and Li, J.P. Heparin - an old drug with multiple potential targets in Covid-19 therapy. *J Thromb Haemost*.(2020)

24. Yang, Y., Du, Y., and Igor A. Kaltashov, I.A. The utility of native MS for understanding the mechanism of action of repurposed therapeutics in COVID-19: heparin as a disruptor of the SARS-CoV-2 interaction with its host cell receptor. BioRxiv, doi.org/10.1101/2020.06.09.142794 (2020)

25. Partridge, L.J., Green, L.R., Monk, P.N. Unfractionated heparin potently inhibits the binding of SARS-CoV-2 spike protein to a human cell line. *bioRxiv***,** 2020.05.21.107870 (2020)

26. Tandon, R., Sharp, J.S., Zhang, F., Pomin, V.H., Ashpole, N.M., Mitra, D., Jin, W., Liu, H., Sharma, P., and Linhardt, R.J. Effective Inhibition of SARS-CoV-2 Entry by Heparin and Enoxaparin Derivatives. *bioRxiv***,** 2020.06.08.140236 (2020)

716 27. Bargellini, I., Cervelli, R., Lunardi, A., Scandiffio, R., Daviddi, F., Giorgi, L., Cicorelli, A.,
717 Crocetti, L., and Cioni, R. Spontaneous Bleedings in COVID-19 Patients: An Emerging
718 Complication. *Cardiovasc Intervent Radiol*, 1-2. (2020)
719 28. Dredge, K., Hammond, E., Handley, P., Gonda, T.J., Smith, M.T., Vincent, C., Brandt, R.,
720 Ferro, V., and Bytheway, I. PG545, a dual heparanase and angiogenesis inhibitor, induces
721 potent anti-tumour and anti-metastatic efficacy in preclinical models. *Br J Cancer* 104, 635-
722 642.(2011)
723 29. Boyango, I., Barash, U., Naroditsky, I., Li, J.P., Hammond, E., Ilan, N., and Vlodavsky, I.
724 Heparanase cooperates with Ras to drive breast and skin tumorigenesis. *Cancer Res* 74,
725 4504-4514.(2014)
726 30. Merad, M., and Martin, J.C. Pathological inflammation in patients with COVID-19: a key role
727 for monocytes and macrophages. *Nat Rev Immunol* 20, 355-362.(2020)
728 31. Khanna, M., Ranasinghe, C., Browne, A.M., Li, J.P., Vlodavsky, I., and Parish, C.R. Is host
729 heparanase required for the rapid spread of heparan sulfate binding viruses? *Virology* 529,
730 1-6.(2019)
731 32. Buijsers, B., Yanginlar, C., de Nooijer, A., Grondman, I., Maciej-Hulme, M.L., Jonkman, I.,
732 Janssen, N.A.F., Rother, N., de Graaf, M., Pickkers, P., Kox, M., Joosten, L.A.B., Nijenhuis,
733 T., Netea, M.G., Hilbrands, L., van de Veerdonk, F.L., Duivenvoorden, R., de Mast, Q
734 & van der Vlag J. Increased plasma heparanase activity in COVID-19 patients. *Front.*
735 *Immunol. doi.org/10.3389/fimmu.2020.57047* (2020)
736 33. Ghanakota, P., and Carlson, H.A. Moving Beyond Active-Site Detection: MixMD Applied to
737 Allosteric Systems. *J Phys Chem B* 120, 8685-8695.(2016)
738 34. Salomon-Ferrer, R., Götz, A.W., Poole, D., Le Grand, S., and Walker, R.C. Routine
739 Microsecond Molecular Dynamics Simulations with AMBER on GPUs. 2. Explicit Solvent
740 Particle Mesh Ewald. *Journal of Chemical Theory and Computation* 9, 3878-3888. (2013).
741 35. Case, D.A., Cheatham Iii, T.E., Darden, T., Gohlke, H., Luo, R., Merz Jr, K.M., Onufriev, A.,
742 Simmerling, C., Wang, B., and Woods, R.J. The Amber biomolecular simulation programs.
743 *Journal of computational chemistry* 26, 1668-1688. (2005).
744 36. Jorgensen, W.L., Chandrasekhar, J., Madura, J.D., Impey, R.W., and Klein, M.L. Comparison
745 of simple potential functions for simulating liquid water. *The Journal of Chemical Physics*
746 79, 926-935. (1983).
747 37. Lindorff-Larsen, K., Piana, S., Palmo, K., Maragakis, P., Klepeis, J.L., Dror, R.O., and Shaw,
748 D.E. Improved side-chain torsion potentials for the Amber ff99SB protein force field.
749 *Proteins* 78, 1950-1958. (2010).
750 38. Kirschner, K.N., Yongye, A.B., Tschampel, S.M., González-Outeiriño, J., Daniels, C.R., Foley,
751 B.L., and Woods, R.J. GLYCAM06: a generalizable biomolecular force field.
752 Carbohydrates. *J Comput Chem* 29, 622-655. (2008).
753 39. Madej, B.D., Gould, I.R., and Walker, R.C. A Parameterization of Cholesterol for Mixed Lipid
754 Bilayer Simulation within the Amber Lipid14 Force Field. *J Phys Chem B* 119, 12424-
755 12435. (2015).
756 40. Gohlke, H., Kiel, C., and Case, D.A. Insights into protein-protein binding by binding free energy
757 calculation and free energy decomposition for the Ras-Raf and Ras-RalGDS complexes. *J*
758 *Mol Biol* 330, 891-913. (2003).
759 41. Genheden, S., and Ryde, U. The MM/PBSA and MM/GBSA methods to estimate ligand-
760 binding affinities. *Expert Opin Drug Discov* 10, 449-461. (2015).
761 42. Onufriev, A., Bashford, D., and Case, D.A. Exploring protein native states and large-scale
762 conformational changes with a modified generalized born model. *Proteins* 55, 383-394.
763 (2004).

43. Micsonai, A., Wien, F., Kernya, L., Lee, Y.H., Goto, Y., Réfrégiers, M., and Kardos, J. Accurate secondary structure prediction and fold recognition for circular dichroism spectroscopy. *Proc Natl Acad Sci U S A* 112**,** E3095-3103.(2015)

Acknowledgments: The authors would like to thank Zucero Therapeutics for provision of pixatimod (PG545) and Queensland Health Forensic & Scientific Services, Queensland Department of Health for provision of QLD02 and QLD935 SARS-CoV-2 isolates.

Funding: V.F. acknowledges support from the Australian Research Council (DP170104431). TB acknowledges support of the Swedish Research Council. AAK acknowledges funding support from the Australian Infectious Diseases Research Centre. Computational (and/or data visualisation) resources and services used in this work were provided by the eResearch Office, Queensland University of Technology, Brisbane, Australia and with the assistance of resources from the National Computational Infrastructure (NCI Australia), an NCRIS enabled capability supported by the Australian Government. N.S.G. is supported through the Advance Queensland Industry Research Fellowship. M.A.S., S.E.G. and C.M-W. acknowledge support of the University of Keele and J.E.T. and E.A.Y. the support of the University of Liverpool. Z.Y. acknowledges the Danish National Research Foundation (DNRF107) and the Lundbeck Foundation, Y-H.C. the Innovation Fund Denmark and R.K. the European Commission (GlycoImaging H2020-MSCA-ITN-721297).

Author contributions: J.E.T., V.F., M.A.S. and K.D. conceived the project. S.E.G., C.J.M-W., N.S.G., J.A.T., K.R.B., N.C., K.N., J.S., Y.X.S., A.A.A., N.M., J.D.J.S., M.C., D.W., P.R.Y., A.A.K., M.A.L., E.A.Y., R.K., Y-H.C., Y.Z., E.T. and M.A.S. designed and conducted the experiments. V.F., E.H., K.D. M.W.C., T.B., M.A.S. and J.E.T. prepared the manuscript.

Competing Interests: E.H. and K.D. are employees of Zucero Therapeutics. V.F., E.H. and K.D. are inventors on pixatimod patents.

Data and materials availability: All data needed to evaluate the conclusions in the paper are present in the paper and/or the Supplementary Materials. Additional data related to this paper may be requested from the authors.

Supplementary Materials

The clinical-stage heparan sulfate mimetic pixatimod (PG545) potently inhibits SARS-CoV-2 virus via disruption of the Spike-ACE2 interaction

Scott E. Guimond, Courtney J. Mycroft-West, Neha S. Gandhi, Julia A. Tree, Karen R. Buttigieg, Naomi Coombes, Kristina Nyström, Joanna Said , Yin Xiang Setoh, Alberto A. Amarilla, Naphak Modhiran, De Jun Julian Sng, Mohit Chhabra, Daniel Watterson , Paul R. Young, Alexander A. Khromykh, Marcelo A. Lima, Edwin A.Yates, Richard Karlsson, Yen-Hsi Chen, Yang Zhang, Edward Hammond, Keith Dredge, Miles W. Carroll, Edward Trybala, Tomas Bergström, Vito Ferro, Mark A. Skidmore and Jeremy E. Turnbull

The file includes:

Table S1
Figs. S1 to S3

Table S1: Amino acids at position 614 in Spike protein of SARS-CoV-2 isolates

Isolate	Amino acids at position 614 in Spike
VIC01	D
QLD02	D
QLD935	G
DE-Gbg20	G

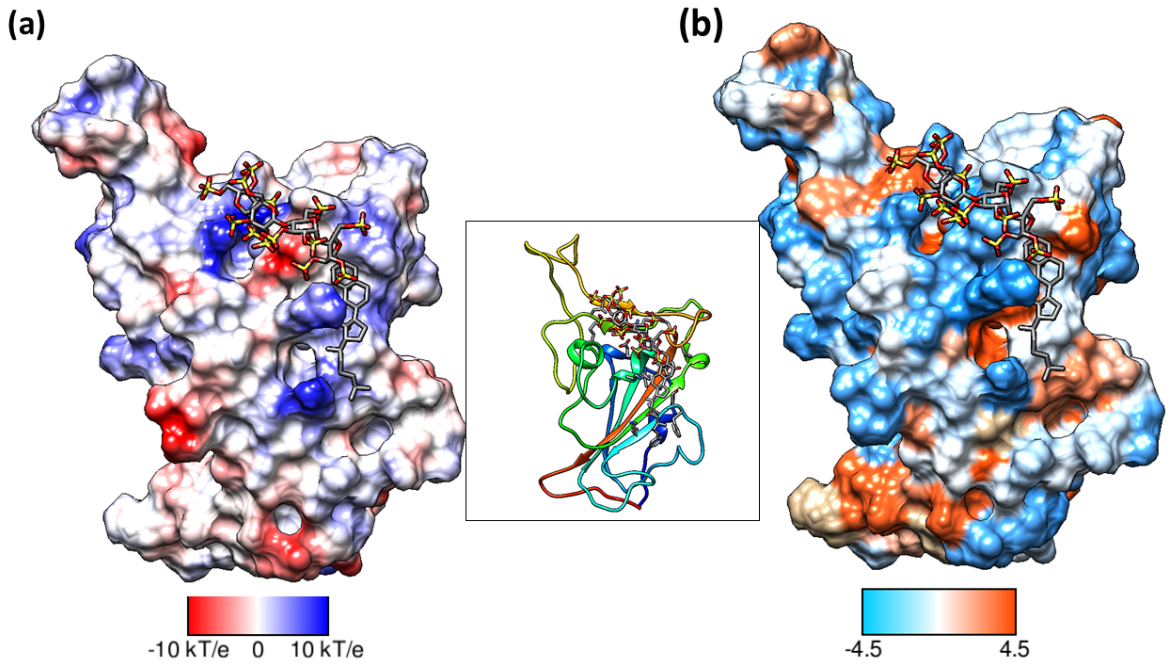

Figure S1. An alternate binding mode of pixatimod on the S1 RBD presented an unfavourable total binding free energy. Surfaces are oriented in the same direction as shown in the ribbon diagram in the inset. (a) Coulombic Surface Coloring defaults: ε = 4r, thresholds ± 10 kcal/mol·e were used. Blue indicates surface with basic region whereas red indicates negatively charged surface. (b) The hydrophobic surface was coloured using the Kyte-Doolittle scale wherein blue, white and orange red colour indicates most hydrophilic, neutral and hydrophobic region, respectively. UCSF Chimera was used for creating surfaces and rendering the images. Hydrogens are not shown for clarity.

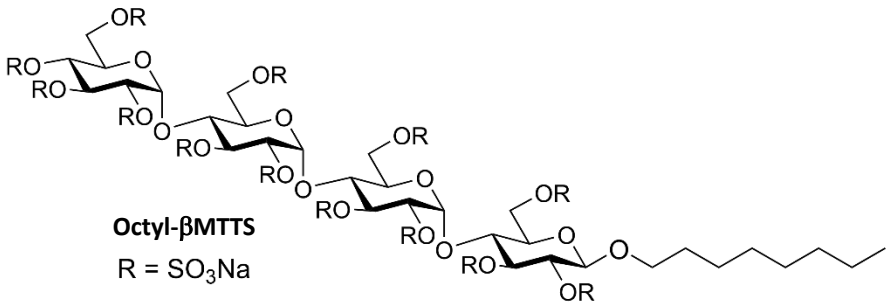

Figure S2. **Structure of octyl β-maltotetraoside tridecasulfate**, an analogue of pixatimod without the steroid side chain.

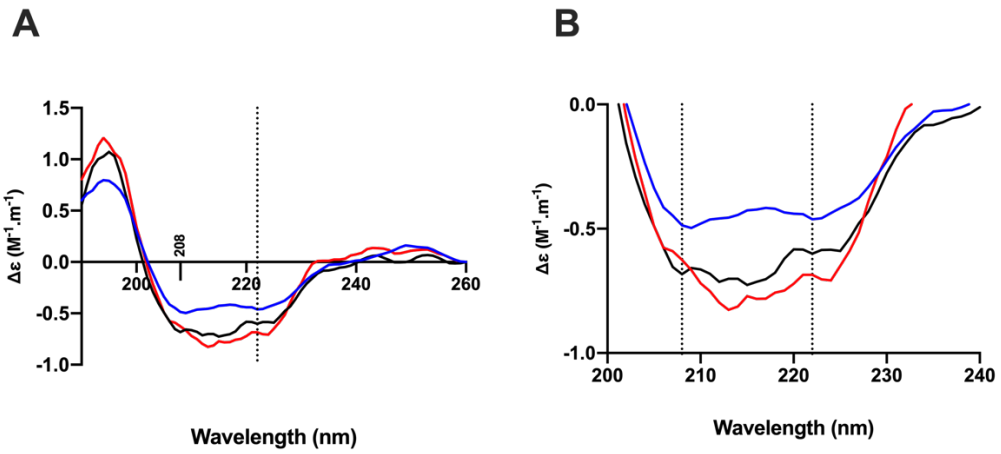

Figure S3: The conformational change of the SARS-CoV-2 S1 RBD observed in the presence of pixatimod by circular dichroism (CD) spectroscopy. (A). Circular dichroism spectra (190 - 260 nm) of SARS-CoV-2 S1 RBD alone (black solid line) and pixatimod (blue solid line) in PBS, pH 7.4. The red line represents the sum of the two individual spectra. Vertical dotted line indicates 222 nm (B) Details of the same spectra expanded between 200 and 240 nm. Vertical dotted lines indicate 222 nm and 208 nm.